

# Physics-informed Blind Reconstruction of Dense Fields from Sparse Measurements using Neural Networks with a Differentiable Simulator

Ofek Aloni<sup>1</sup> Barak Fishbain<sup>2</sup>

## Abstract

Generating dense physical fields from sparse measurements is a fundamental question in sampling, signal processing, and many other applications. State-of-the-art methods either use spatial statistics or rely on examples of dense fields in the training phase, which often are not available, and thus rely on synthetic data. Here, we present a reconstruction method that generates dense fields from sparse measurements, without assuming availability of the spatial statistics, nor of examples of the dense fields. This is made possible through the introduction of an automatically differentiable numerical simulator into the training phase of the method. The method is shown to have superior results over statistical and neural network based methods on a set of three standard problems from fluid mechanics.

## 1. Introduction

Inferring dense fields from sparse measurement is a fundamental phase in many scientific and engineering applications, as the number of sensors and spatiotemporal resolution of measurement is often limited. Examples of this task include the reconstruction of dense air pollution maps from distant measuring stations (Nebenzal et al., 2020), radar measurements of precipitation (Mishra et al., 2014), and surface elevation maps in ocean waves (Ehlers et al., 2023). This data scarcity motivates the use of post-hoc methods to approximate the full field of values from the available measurements.

Inverse problems of this nature, reconstruction of the dense field from sparse measurements, are inherently ill-posed, as multiple potential fields can correspond to the same sparse measurements. This ambiguity makes the domain a natural

candidate for Machine Learning (ML) methods, which can learn to generate physically plausible solutions by capturing complex non-linear priors (Karniadakis et al., 2021).

Classical reduced-order modeling techniques, such as Proper Orthogonal Decomposition (POD) and Dynamic Mode Decomposition (DMD), provide established frameworks for reconstructing state fields from sparse sensors (Schmid, 2010). These methods, particularly the Gappy POD approach (Everson & Sirovich, 1995), operate by constructing a low-dimensional basis from a pre-computed library of full-field snapshots. The sparse observations are then projected onto this basis to resolve the ill-posed nature of the problem. These data-driven methods depend fundamentally on the availability of high-fidelity data.

Kriging spatial interpolation (or Gaussian Process Regression) is another classic statistical approach for dense field reconstruction (Cressie, 1993). Kriging provides the Best Linear Unbiased Predictor (BLUP) based on the spatial autocorrelation of the data, modeled via a variogram. While effective for stationary fields with well-behaved statistical properties, Kriging struggles with complex, non-linear changes in the sampled field. As it relies purely on statistical relationships between points, it can be applied to sparse measurements directly. However, it ignores the underlying physical laws that govern the field's evolution.

An example of an ML approach for reconstruction is in Fukami et. al (2021). In their work, a Convolutional Neural Network (CNN) is employed to interpolate spatial data acquired in fluid dynamics problems, such as the vorticity field in a two-dimensional cylinder wake. The methodology proposed involves pre-processing the sampled data through the construction of Voronoi tessellations.

Recent advancements in this domain have employed generative diffusion models, drawing upon their demonstrated efficacy in synthesizing image and video data, e.g. (Amorós-Trepat et al., 2025). An important merit of diffusion models lies in their capacity to perform stochastic sampling from a distribution of plausible outcomes, as opposed to the deterministic outputs characteristic of conventional machine learning models. A prominent illustration of this methodology is embodied in the DiffusionPDE framework (Huang

<sup>1</sup>Department of Mathematics, Technion, Haifa, Israel

<sup>2</sup>Department of Civil and Environmental Engineering, Technion, Haifa, Israel. Correspondence to: Ofek Aloni <ofek.aloni@campus.technion.ac.il>, Barak Fishbain <fishbain@technion.ac.il>.

et al., 2024). The DiffusionPDE system accepts as input two spatially sampled images, typically representing the initial and terminal states of a system, and concurrently generates predictions for both states. Within this framework, the generated predictions reconstruct the complete initial and final fields.

These approaches are fundamentally constrained in practical applications, as a completely resolved field is typically unavailable to serve as ground truth for model training. Consequently, the prevailing strategy involves the use of simulated data for training purposes, wherein fully resolved fields can be sampled at the measurement locations. Although this method can produce fields that replicate similar physical behavior, the resulting initial conditions are not necessarily representative of those in the actual system.

To date, there have been limited efforts aimed at addressing the gap in ground truth data. For instance, (Ehlers et al., 2025) investigated this challenge within the context of ocean waves by employing a Physics Informed Neural Operator (PINO). In that study, the PINO is trained to reconstruct nonlinear wavefields in a single spatial dimension, utilizing only sparse buoy or radar measurements. Notably, the experimental framework incorporates buoy measurements solely as data loss, thereby refraining from introducing additional information when buoy measurements serve as input. Consequently, the learning process is driven exclusively by the physics-based loss terms.

Following this line of research, we introduce here a method for training an ML model for dense flow field reconstruction, using only the sampled values in different time steps. The core innovation is incorporating existing knowledge of the physical process inside the *training loop*, by incorporating a differentiable numerical PDE simulator (Thurey et al., 2021). This way, the ML model is enabled to learn directly from the target data, while being exposed to the physics of the problem, and correcting itself accordingly. This eliminates the need to generate and train on synthetic samples, and reduces the need for additional constraints on the optimization process, as is the case in Physics Informed Neural Networks (PINNs) (Raissi et al., 2017). We refer to our method as Physics-informed Blind Reconstruction (PhysBR).

## 2. Methodology

### 2.1. Problem Formulation

Let  $\Omega \subseteq \mathbb{R}^d$  be the spatial domain of interest. The goal is to infer a spatiotemporal measurement field, given by an underlying function  $u(t, x) : \mathbb{R}^+ \times \Omega \rightarrow \mathbb{R}^{d'}$ , that is a solution to some PDE in both time and space:

$$F(u, \frac{du}{dt}, \frac{d^2u}{dt^2}, \nabla u, \nabla^2 u \dots) = 0$$

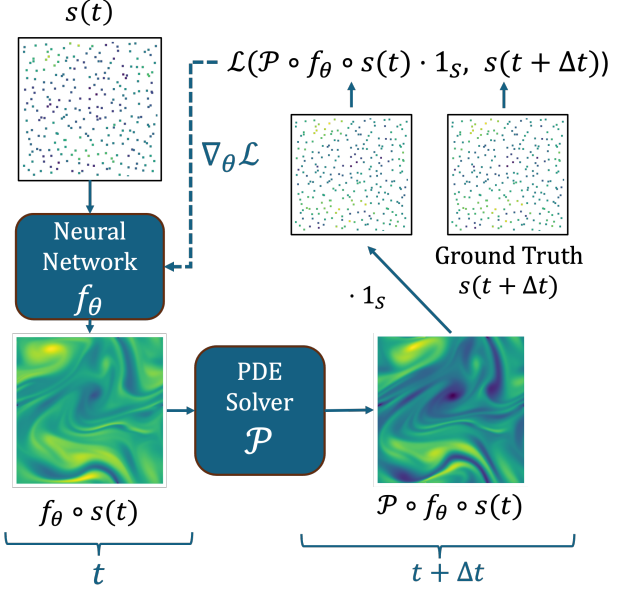


Figure 1. PhysBR training loop - schematic displaying the pipeline for learning the weights in  $f_\theta$ . First, an initial dense field is generated from the sparse samples  $s(t)$  using the neural network  $f_\theta$ . Then, it is advanced in time using the differentiable numerical solver  $\mathcal{P}$ . Finally, it is sampled by multiplication with  $\mathbb{1}_S$ , and loss is compared relative to the ground truth field values at sample locations  $s(t + \Delta t)$ .

With some boundary conditions  $u|_{\partial\Omega}$ .

In the following, it is assumed that  $F$  and  $u|_{\partial\Omega}$  are known, but  $u(t, x)$  is not. Instead, there is a set of  $m$  fixed points in the domain,  $S \subset \Omega$  in which the value of  $u$  is measured, while in the rest of  $\Omega$  it is unknown. The sparse observations are represented as  $s(t) := u(t, x) \cdot \mathbb{1}_S$ , where  $\mathbb{1}_S$  is the indicator function:

$$\mathbb{1}_S(x) = \begin{cases} 1, & x \in S, \\ 0, & \text{otherwise} \end{cases}$$

Let  $\mathcal{U}$  denote the space of spatial fields  $f : \Omega \rightarrow \mathbb{R}^{d'}$ , representing possible states of the system at any fixed time.

For the reconstruction tasks, we would like to deduce a reconstructing model,  $M : \mathcal{U} \rightarrow \mathcal{U}$  that, given a sparse measurement  $s(t)$ , returns an approximation of the full field:

$$M \circ s(t) \approx u(t, \cdot) \quad (1)$$

Note again that the problem of reconstruction is ill-defined. There could be two solutions  $u, v \in \mathcal{U}$  of the PDE  $F$ , such that  $u \neq v$ , but  $u \cdot \mathbb{1}_S = v \cdot \mathbb{1}_S$ . Thus, a recovery of the full field without additional assumptions or information is impossible. We can, however, attempt to construct  $M$  such that  $M \circ s \in \mathcal{U}$  are physically consistent fields, with minimal errors compared to the true  $u(t)$  from which  $s(t)$  was sampled.

## 2.2. Construction of the Reconstructor

The sole input to the process is  $s(t)$ , with no samples of the entire field,  $u(t, \cdot)$ , known. Hence, implementing  $M$  as a Neural Network (NN) so  $s(t)$  is the input and  $u(t, \cdot)$  is the output to train against, is not applicable as the sample space  $\mathcal{X} = \{s(t_i)\}_{i=1}^N$  is available, but the target space  $\mathcal{Y} = \{u(t_i, \cdot)\}_{i=1}^N$  is not. Thus, we cannot compute the data loss  $\mathcal{L}(M \circ s(t), u(t, \cdot))$  and are unable to learn an approximate reconstructor directly.

To this end our novel method, which relies on a differential PDE solver, allows training the NN solely on pairs of an initial measurement  $s(t)$ , and a later measurement  $s(t + \Delta t)$ , where  $\Delta t$  is a small time increment.

In this way, given a sparse measurement  $s(t)$ , the reconstructor  $\mathcal{M}$  returns an approximation of the full field at  $t + \Delta t$ :

$$\mathcal{M} \circ s(t) \approx u(t + \Delta t, \cdot) \quad (2)$$

Then the loss is computed *only at the measuring points* at time  $t + \Delta t$ :

$$\mathcal{L}((\mathcal{M} \circ s(t)) \cdot \mathbb{1}_S, s(t + \Delta t, \cdot)) \quad (3)$$

In this formulation, if no PDE solver is integrated into the reconstruction framework, a NN  $\mathcal{M} = f_\theta$ , that is trained so it minimizes the above loss function, would provide an approximation of the dense field in samples' locations in the next time step,  $\mathcal{M} \circ s(t) \approx s(t + \Delta t)$ , rather than satisfying Eq. 2 as desired. This limitation motivates the joint employment of the neural network and the PDE solver: the network estimates the unobserved dense field, while the solver propagates it to a future state where supervision is available.

Recall that it is assumed that  $F, u|_{\partial\Omega}$  are known, and so it is possible to implement a numerical PDE solver  $\mathcal{P} : \mathcal{U} \rightarrow \mathcal{U}$ :

$$\mathcal{P}(u(t, \cdot); F, u|_{\partial\Omega}) \approx u(t + \Delta t, \cdot) \quad (4)$$

Combining the two, the solver  $\mathcal{P}$  and the NN,  $f_\theta$ , we obtain:

$$\mathcal{M} := \mathcal{P} \circ f_\theta \quad (5)$$

Note that the solver  $\mathcal{P}$  is applied during inference as well, and not only during training. This has the advantage of enforcing physical constraints (e.g. incompressibility).

Fig. 1 gives an overview of a single iteration of the training process of  $f_\theta$ . First, reconstructing an initial field from  $s(t)$  using  $f_\theta$ , and advancing in time using the simulator  $\mathcal{P}$ . Then, the approximate reconstruction is sampled via multiplication with  $\mathbb{1}_S$ , and loss is computed relative to the ground truth, namely the sampled values  $s(t + \Delta t)$ .

Finally,  $\nabla_\theta \mathcal{L}$  is computed, backpropagating through  $\mathcal{P}$ , and the weights  $\theta$  are updated accordingly.

In practice, as a preprocessing step, the sparse samples  $s(t_0) = u(t_0, \cdot) \mathbb{1}_S$  are mapped to Voronoi tessellations (Fukami et al., 2021).

A mechanism to encourage  $f_\theta$  to output smooth, physically feasible fields is penalizing large spatial gradients of the output via an additional loss term. Given a tunable hyperparameter  $\lambda \geq 0$ , the loss function becomes:

$$\mathcal{L}_{reg} = \|\nabla_x [f_\theta \circ s(t)](x)\|_2^2, \quad \mathcal{L}_{tot} = \mathcal{L} + \lambda \cdot \mathcal{L}_{reg} \quad (6)$$

The methodology presented herein is inherently *model agnostic*. Any trainable function  $f_\theta$  may be employed, provided that the corresponding input and output dimensions are suitably defined.

In practice, computing the gradients that are needed to update the weights of  $f_\theta$  during training relies on automatic differentiation (Baydin et al., 2018). In this respect, an important practical consideration is that  $\mathcal{P}$  must be differentiable, to allow for backpropagation through the solver. There is an increasing number of solutions built to address this demand, such as PhiFlow (Holl & Thuerey, 2024).

An important note is the applicability of PhysBR to chaotic systems, where the trajectory of the solution  $u$  in the phase space is highly sensitive to changes in initial condition. The rate of divergence of similar initial conditions is often quantified using the (largest) Lyapunov exponent  $\lambda \in \mathbb{R}$  (Strogatz, 2024). Chaotic systems are characterized by  $\lambda > 0$ . In those cases, there is a bound on the sampling interval  $\Delta t$  when applying PhysBR:

$$\Delta t < \frac{1}{\lambda} \quad (7)$$

Otherwise, even a close to perfect reconstruction of initial field  $f_\theta(s(t))$  will result in large values of loss  $\mathcal{L}$  (Eq. 3), undermining the optimization process. While exact calculation of  $\lambda$  is non-trivial, the practical takeaway is that  $\Delta t$  should be small compared to timescales in the given system.

## 2.3. Case Studies

The performance of PhysBR is evaluated on a number of three classical fluid mechanics problems: 1D Burgers' Equation (Whitham, 1999), Wake flow (bounded Navier-Stokes with obstacle) (Wu, 1972), and Kolmogorov Flow (unbounded Navier-Stokes with periodic forcing) (Thess, 1992).

### 2.3.1. BURGERS' EQUATION

For a given field  $u(x, t)$  and diffusion coefficient (or kinematic viscosity)  $\nu$ , the general form of the viscous Burgers' equation in one spacial dimension is:

$$\partial_t u = \nu \partial_{xx} u - u \partial_x u \quad (8)$$

In the simulated data,  $\nu = 0.1$ , and periodic boundary conditions were used. The spatial domain was  $\Omega = [0, 1]$  with resolution 256. 5,000 initial conditions  $u(t, x)$  were generated using Gaussian Random Fields (GRFs), as in (Li et al., 2021), and  $u(t + \Delta t, x)$  was simulated with  $\Delta t = 0.01$ . Diffusion and semi-lagrangian advection were computed using the PhiFlow library with PyTorch backend (Holl & Thuerey, 2024). The number of samples was  $|S| = 16$ , uniformly spaced.

### 2.3.2. WAKE FLOW (BOUNDED NAVIER-STOKES WITH OBSTACLE)

Here, incompressible flow in two dimensions with an obstacle is considered, sometimes known as Wake flow. In this setup, flow around a fixed cylinder positioned as an obstacle inside the domain is considered. We observe the velocities  $\mathbf{u}(x, y, t) = (u(x, y, t), v(x, y, t))$ . The two-dimensional Navier-Stokes equations are of the form:

$$\partial_t \mathbf{u} + \mathbf{u} \cdot \nabla \mathbf{u} = \nu \nabla^2 \mathbf{u} - \frac{1}{\rho} \nabla \mathbf{p} \quad (9)$$

With the additional constraint  $\nabla \cdot \mathbf{u} = 0$  due to incompressibility. Note that the pressure  $\mathbf{p}$  is dependent on  $\mathbf{u}$ .

Data was generated by a numerical simulation with density  $\rho = 1$ , and viscosity  $\nu = 10^{-5}$ . A square  $[0, 1] \times [0, 1]$  domain was discretized as  $64 \times 64$ . The cylinder obstacle's radius was  $R = 0.075$ , centered at  $(0.5, 0.7)$ . Constant velocity on the upper boundary was set  $v(y = 1) = -0.02$ , with a zero gradient boundary condition on the outflow  $y = 0$ . Overall, the Reynolds number of such a setup, based on the cylinder diameter, is:

$$Re = \frac{v_{\text{free}} \cdot 2R}{\nu} = \frac{0.02 \cdot 0.15}{10^{-5}} = 300$$

In this range, periodic vortex shedding can be seen (Wu, 1972). The simulated system ran for 500 warmup steps. The data consists of 5,000 pairs with time difference  $\Delta t = 0.01$ , with a step of 1 between one initial condition and the next. Simulation using semi-lagrangian advection, explicit diffusion, and incompressibility enforcing was implemented using PhiFlow.

The sample locations  $S$  the sensors were chosen non-uniformly, as the problem is not symmetric in  $\hat{y}$ , and spatial variation is high within the vortex shedding and around the

cylinder. Entropy across the generated fields was used to select sensor locations (Mano et al., 2022), while ensuring non were placed inside of the cylinder obstacle. All locations on the outside perimeter of the cylinder were also included. Overall, the number of sample locations was  $|S| = 247$ .

Note that using PhysBR, the condition  $\mathbf{u} \equiv 0$  inside the obstacle is inherently enforced via the simulator  $\mathcal{P}$ . There is no built-in way to enforce this in any of the other compared methods (see section 2.4). However, to evaluate the performance differences in non trivial parts of the domain, the velocity in the interior was set to zero post hoc, in all reconstructions.

### 2.3.3. KOLMOGOROV FLOW (UNBOUNDED NAVIER-STOKES WITH PERIODIC FORCING)

Here, the problem is two-dimensional incompressible flow with periodic boundary conditions, and periodic forcing in one of the axes:

$$\partial_t \mathbf{u} + \mathbf{u} \cdot \nabla \mathbf{u} = \nu \nabla^2 \mathbf{u} - \frac{1}{\rho} \nabla \mathbf{p} + c \sin(ky) \hat{x} \quad (10)$$

Where  $c > 0$  is a scale factor, and  $k \in \mathbb{N}$  is the forcing wavenumber.

In this setup, it is natural to observe the scalar vorticity field  $\omega := \nabla \times \mathbf{u}$  rather than the velocities  $\mathbf{u}$  directly, since the velocities can be recovered from  $\omega$ , using stream functions. Hence, there exists a scalar  $\psi(t, x, y)$  such that:

$$u = \frac{\partial \psi}{\partial x}, v = -\frac{\partial \psi}{\partial y}$$

Which means to recover  $\mathbf{u}$  from  $\omega$ , the following Laplace equation need to be solved:

$$\omega = \nabla \times \mathbf{u} = -\nabla^2 \psi$$

With the periodic boundary conditions and no obstacles this is straightforward to solve numerically. This is advantageous for testing reconstruction, as only a single channel is to be reconstructed (and not two, as in Wake flow).

A  $[0, 1] \times [0, 1]$  domain with resolution of  $256 \times 256$  was chosen. Data was generated using  $\rho = 1, \nu = 10^{-3}$ , forcing with scale factor  $c = 100$  and wavenumber  $k = 8$ , using time increment  $\Delta t = 0.001$ . The simulator was implemented directly in PyTorch, using a spectral approach based on the algorithm in (Koehler, 2024). After 500 warmup steps, 5,000 consecutive samples were saved. Sample locations are uniformly spread in the domain. Models are separately trained and evaluated on two measurement densities  $|S| = 3, 200$ , and  $|S| = 256$ .

## 2.4. Comparison Methods

The novelty of PhysBR lies in its training procedure, which uses solely data from the sample locations, and no full-field

Table 1. Mean relative  $L^2$  error of the reconstruction  $\pm$  standard deviation, for each of the different test cases - the PhysBR model, baseline CNN, Kriging, IDW, and, RBF. Calculated on an the PhysBR test set containing 500 samples. Lowest error in bold. As can be seen, PhysBR is the most consistent, achieving the lowest error in all test cases.

	<b>PHYSBR</b>	CNN	KRIGING	IDW	RBF
BURGERS	<b><math>0.06 \pm 0.03</math></b>	$0.4 \pm 0.1$	$0.22 \pm 0.17$	$0.16 \pm 0.04$	<b><math>0.06 \pm 0.03</math></b>
WAKE FLOW	<b><math>0.059 \pm 0.002</math></b>	$0.145 \pm 0.004$	$0.078 \pm 0.003$	$0.108 \pm 0.002$	$0.064 \pm 0.003$
KOLMOGOROV, $ S  = 3,200$	<b><math>0.12 \pm 0.02</math></b>	$0.14 \pm 0.02$	$0.3 \pm 0.2$	$0.198 \pm 0.017$	<b><math>0.12 \pm 0.02</math></b>
KOLMOGOROV, $ S  = 256$	$0.48 \pm 0.04$	$0.70 \pm 0.04$	$0.6 \pm 0.2$	$0.50 \pm 0.04$	<b><math>0.45 \pm 0.05</math></b>

data. This poses a challenge in comparing to existing state-of-the-art ML models for reconstruction, as those use the entire field for the training task. This limits the available options for fair benchmarking.

For this reason, as a baseline, we train a CNN with identical architecture using leave-some-out on the sample locations.  $S$  is decomposed as  $S = S_{in} \cup S_{loss}$ . 70% of sample locations are contained in  $S_{in}$ , and used as inputs to the model. The rest are in  $S_{loss}$ , and are used for computing the data-driven loss term. In contrast to PhysBR, both input and ground truth are sampled from the same measurements, i.e. from  $s(t + \Delta t)$ . Smoothness regularization is added to the data loss, as in Eq. 6, and the parameter  $\lambda$  is tuned. Voronoi preprocessing is done here as well. Overall the loss is:

$$\mathcal{L}_{\text{baseline}} = \| [f_\theta \circ (s(t + \Delta t) \cdot \mathbf{1}_{S_{in}}) - s(t + \Delta t)] \cdot \mathbf{1}_{S_{loss}} \|_2^2 + \mathcal{L}_{\text{reg}}$$

The CNN architecture was kept identical to the one used by the PhysBR model.

In addition to this learned baseline, the method is compared to classical methods for reconstruction of spatial data. There, reconstruction from the sparse samples is based on spatial correlations in the sampled fields, and in particular does not require any training examples.

The first, simplest baseline is Inverse Distance Weighting (IDW). IDW is a deterministic method that assumes values at unsampled locations are a distance-weighted average of the available samples. For an arbitrary point  $x \in \Omega$ , the reconstructed value  $\hat{u}(x)$  is given by:

$$\hat{u}(x) = \frac{\sum_{x_i \in S} w_i u(x_i)}{\sum_{x_i \in S} w_i}, \quad w_i = \frac{1}{\|x - x_i\|_2^p} \quad (11)$$

where  $p > 0$  is a power parameter controlling the rate of decay. Note that taking the limit of  $p \rightarrow \infty$  is equivalent to computing the Voronoi tessellation, as is done in the preprocessing step. In Burgers and Kolmogorov,  $p = 3$ , and in Wake flow,  $p = 4$ , selected to minimize  $L^2$  error.

The second baseline is Kriging, also known as Gaussian Process Regression (Cressie, 1993). It relies on the spatial auto-correlation of the data, treating the field  $u$  as a realization of a stochastic process composed of a deterministic trend  $\mu(x)$  and a stochastic residual  $\varepsilon(x)$ . The method provides the

Best Linear Unbiased Predictor (BLUP) by solving a system of linear equations based on a modeled semi-variogram. A typical distinction is between Ordinary Kriging, which assumes the underlying trend  $\mu(x)$  is constant but unknown (stationary mean), and Universal Kriging, which relaxes this assumption by modeling  $\mu(x)$  as a polynomial function of the spatial coordinates. The latter allows the model to account for systematic spatial drifts that may be present in the data. Another important choice is of the functional form of the variogram model, e.g. gaussian, linear, exponential, and more.

Interpolation and fitting of the variogram is done using PyKrig (Murphy et al., 2025). For wake flow, universal kriging with a spherical variogram model is used, while for Kolmogorov, Ordinary Kriging with exponential variogram. In Burgers, a 1d Ordinary Kriging with spherical variogram is used. In every instance, the variogram model and Kriging type were selected to minimize  $L^2$  error.

Another baseline considered is Radial Basis Function (RBF) interpolation (Buhmann, 2003). RBF methods reconstruct a continuous field by expressing it as a weighted sum of radially symmetric basis functions centered at the sample locations. Given sparse samples  $(x_i, u(x_i))_{x_i \in S}$ , the reconstructed field is written as

$$\hat{u}(x) = \sum_{x_i \in S} \alpha_i \phi(\|x - x_i\|_2)$$

where  $\phi(r)$  is a chosen radial kernel and the coefficients  $\alpha_i$  are determined by enforcing interpolation at the sample locations. The weights are obtained by solving a linear system.

In the present work, reconstruction with RBF is performed using the RBFInterpolator implementation in SciPy (Virtanen et al., 2020), with a thin plate spline kernel.

## 2.5. Training Procedure

PyTorch (Ansel et al., 2024) is used to carry out the experiments. For the 2d cases  $f_\theta$  is a U-net CNN with self-attention (Oktay et al., 2018). For the 1d case, a simple 1d CNN, with 7 layers, each with 48 filters, and kernel size of 16. In all cases, the loss function is the Mean Square Error (MSE), and training is conducted with the Adam optimizer

(Zhang, 2018).

To mitigate the risk of exploding gradients, weights were initialized with uniform Xavier initialization (Glorot & Bengio, 2010), with gain of 0.1, and gradients were clipped before update of the model’s weights.

Since regularization loss is used, the parameter  $\lambda$  in Eq. (6) is tuned, along with learning rate and batch size. Tuning is done with Optuna (Akiba et al., 2019), conducting up to 20 trial runs with limited training time to find an optimum. This was done for both PhysBR and the CNN baseline.

All training and testing procedures were conducted on a local Windows-based workstation equipped with an Intel i7 9700 8-core CPU and 96 GB of RAM. CUDA was utilized to leverage an NVIDIA GeForce RTX 2060 GPU with 8 GB of memory.

### 3. Results

The performance of each reconstruction model across the various test cases is summarized in Table 1. For each scenario, 5000 realizations are generated under varying initial conditions. These realizations are subsequently partitioned into training, validation, and test sets. The models are first trained on the training data, after which each sample in the test set, denoted as  $\{s(t_i)\}_{i=1}^{500}$ , is reconstructed using the trained model. The reconstruction performance of PhysBR and all comparative methods is assessed via the relative error with respect to the ground truth fields; specifically, for a reconstruction  $\hat{u}$  of  $u$ , the scalar  $\frac{\|\hat{u}-u\|_2}{\|u\|_2}$  is evaluated. The values reported represent the mean relative error  $\pm$  standard deviation across all reconstructions.

PhysBR and RBF consistently achieved the lowest mean relative errors in all evaluation scenarios. In particular, both methods exhibited identical errors in the Burgers and Kolmogorov cases with  $|S| = 3,200$ . However, for Wake flow, PhysBR demonstrated an 8.5% lower mean error, whereas RBF outperformed PhysBR by 6% in Kolmogorov with  $|S| = 256$ . The performance disparity in the Wake scenario is especially pronounced; it should be recalled that errors in Table 1 are computed after the zero velocity condition in RBF is manually imposed (2.3.2). In the absence of this constraint, the velocity field inside the cylinder is non-zero, resulting in a mean relative error of 0.09, which constitutes a 56% increase compared to PhysBR.

In the Kolmogorov case with a large number of samples, the CNN baseline yields a lower average error than both IDW and Kriging; however, its error is higher with a smaller sample size and in the Wake flow scenario. While Kriging is capable of attaining low errors, its performance is notably inconsistent, as reflected by the relatively large standard deviations observed in both the Burgers and Kolmogorov

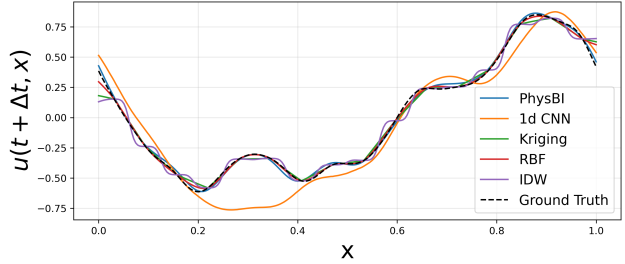


Figure 2. 1d Burgers equation - reconstruction of a single sample  $s(t)$  from the test set by the each method, compared to the ground truth  $u(t + \Delta t, x)$ .

cases. For Kolmogorov with  $|S| = 3,200$ , the minimum test set error is 0.09, the maximum reaches 1, and the median error is 0.16.

For the Burgers equation, Fig. 2 illustrates the reconstruction of a single sample  $s(t + \Delta t)$  from an initial sample  $s(t)$  by each method. PhysBR, RBF, and Kriging closely follow the ground truth across most of the domain. Notably, near the boundaries  $x = 0, 1$ , PhysBR aligns more closely with the true field than the other approaches. The CNN baseline fails to capture certain features of the original signal, most prominently the local maxima near  $x = 0.3$ , which is attributed to the lower number of sample locations provided as input. IDW displays oscillatory behavior around the sample values but does not replicate the underlying field trends.

To provide a detailed visualization of the reconstructions in the Wake flow scenario, Fig. 3 presents the vorticity  $\omega = \nabla \times \mathbf{u}$  associated with a single velocity field  $\mathbf{u}(t + \Delta t, x, y)$ , as reconstructed by PhysBR and the comparison methods. Unlike the Kolmogorov case, where  $\omega$  is the directly measured and reconstructed variable, here the velocity field is reconstructed, and vorticity is displayed for visualization purposes only. The phenomenon of vortex shedding (depicted in blue, below the cylinder) is evident across all reconstruction techniques; however, the finer structures are most accurately recovered by PhysBR. While the Kriging method produces a smoother reconstruction above the cylinder, it does not successfully capture the triangular feature below the cylinder, visible in red. The CNN reconstruction exhibits a noticeable artifact at the lower boundary of the reconstruction. In the case of IDW, the reconstruction reveals a distinct point pattern localized around the sample positions.

Fig. 4 presents a comparative analysis of the reconstruction of the vorticity  $\omega$  in the Kolmogorov scenario, utilizing various methodologies. The identical ground truth field  $\omega(t + \Delta t)$  is reconstructed twice for each approach: once with a high sample density ( $|S| = 3,200$ ) and once with a lower sample density ( $|S| = 256$ ), as depicted in the top

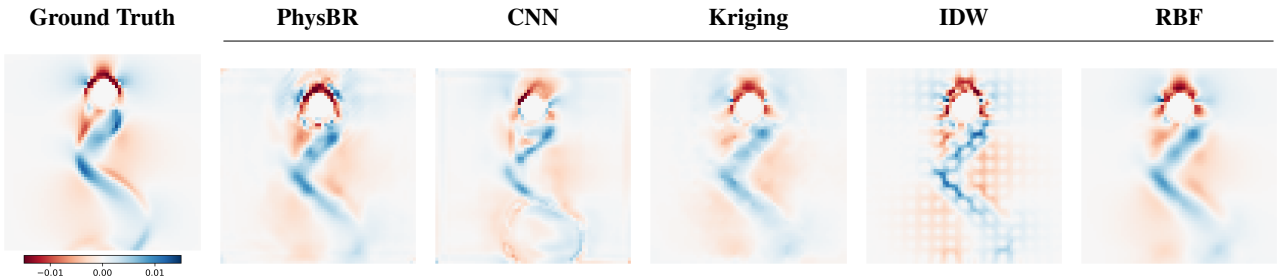


Figure 3. Wake flow (Incompressible flow with obstacle) - visual comparison between the vorticity  $\omega = \nabla \times \mathbf{u}$  of reconstructions of  $\mathbf{u}(t + \Delta t, x, y)$  using different methods, compared to the ground truth. Vorticity is shown for visualization only. Heatmap range is fixed in all subplots according to the ground truth.

and bottom rows, respectively.

At elevated sample densities, the reconstructions produced by PhysBR, CNN, and RBF appear, at first inspection, nearly indistinguishable from the ground truth. However, upon closer examination, all three methods exhibit less smoothness relative to the true field, a phenomenon particularly evident in the thin horizontal or spiraling regions of pronounced vorticity.

While PhysBR achieves superior reconstruction accuracy, it incurs a higher computational cost than a pure neural network due to the integration of the differentiable solver within the training loop and during inference. Average training time per epoch and total inference time on the test set (500 samples) was compared against the CNN without the solver. For the Wake flow dataset, PhysBR required approximately 12.75 minutes per epoch compared to 5.7 minutes for the CNN. In the Kolmogorov case, 1.59 hours vs. 1.19 hours per epoch, and in Burgers, 14 seconds vs. 0.66 of a second. Inference latency was also higher for PhysBR; for example, processing the Wake flow test set took 47 seconds, whereas the CNN completed the task in roughly one second. In Kolmogorov, inference time was 16 seconds for the PhysBR model, and 3.6 seconds for the CNN baseline.

## 4. Discussion

The results presented in Table 1 demonstrate that PhysBR achieves superior and more consistent performance on the test data compared to the CNN baseline, IDW, and Kriging, while remaining competitive with RBF. Importantly, it should be emphasized that the CNN component within PhysBR is never directly exposed to the target values during training. Exposing the model to targets would undermine the foundational principle of learning from data. The fact that PhysBR attains competitive results across all scenarios, consistently, underscores the strength and robustness of the approach.

Across all case studies, PhysBR incorporates additional

information from the underlying PDE into the reconstruction process, beyond merely leveraging the sample point values  $s(t)$ .

First, in Fig. 2, PhysBR successfully maintains periodic boundary conditions, even in the absence of sensor placements at the domain boundaries. In contrast, the baseline methods deviate from the true field, highlighting PhysBR’s ability to respect physical constraints.

Second, for the Kolmogorov case with  $|S| = 256$  (see Fig. 4), the reconstructed vorticity field by PhysBR preserves physical structures, such as rotation and curvature within the underlying Voronoi tessellations, in contrast to the rigid grid-like output from IDW. Notably, for this setting, RBF achieves a lower error than PhysBR, indicating an opportunity for further improvement. With fewer measurements, the Voronoi tessellations in the input data become more pronounced in the results. This observation motivates future work to explore alternative preprocessing techniques or architectures with stronger inductive biases, aiming to enhance reconstruction accuracy in low-data regimes.

Finally, in the Wake flow case, PhysBR provides an integrated approach for handling non-trivial internal boundaries within the domain. Additionally, it surpasses the compared methods in terms of relative error. These results suggest that PhysBR is particularly well-suited for reconstructing fields with complex geometries, which is especially advantageous for real-world applications such as modeling flow in urban environments.

The increase in training and inference time for PhysBR compared to using solely CNN is notable. Incorporating a numerical simulator incurs a computational cost that is highly dependent on the complexity of the observed system, the PDE solver, and the desired resolution. Nevertheless, in this study, the computational overhead remained within manageable limits on consumer-grade hardware, and was not a prohibiting factor.

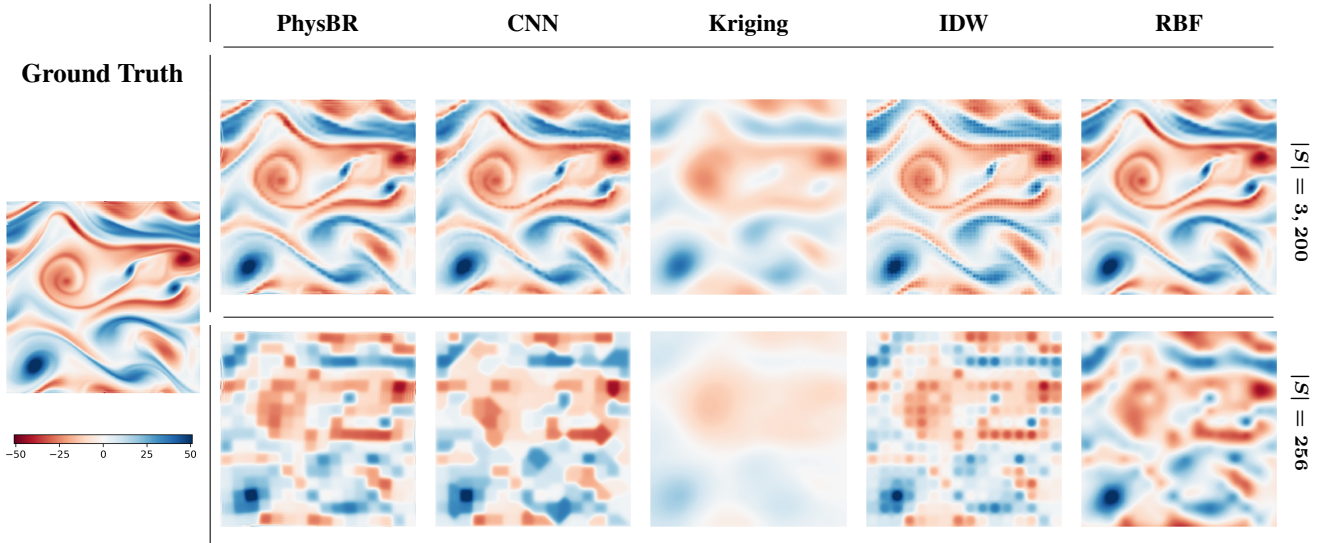


Figure 4. Visual comparison of Kolmogorov Flow reconstruction. The left panel shows the ground truth vorticity field. The table compares PhysBR and the other four reconstruction methods. In the top row there are  $|S| = 3,200$  sample locations, and on the bottom row  $|S| = 256$ . Heatmap range is fixed in all subplots according to the ground truth.

## 5. Conclusion

In this work, we have introduced PhysBR, a framework that integrates a differentiable PDE solver within the training loop of a neural network, thereby enabling the reconstruction of complete fields from sparse measurements without requiring access to ground-truth data. Through comprehensive case studies in fluid mechanics, we demonstrate that PhysBR consistently outperforms conventional baselines such as CNNs, Kriging, and IDW, while achieving performance comparable to RBF methods.

For future research, we suggest that extending the framework to diffusion models, though non-trivial, presents a promising avenue for stochastically sampling high-quality full fields. Moreover, generalizing the input and/or output to encompass measurements across multiple timesteps may further enhance the accuracy and broaden the applicability of the proposed methodology.

A persistent and significant challenge in applying machine learning methods to measurement data, or any data with underlying physical meaning, is the scarcity of available data, particularly when contrasted with more commonly studied modalities such as text, images, and videos. The approach presented herein addresses this issue by providing a principled method to exploit (spatially) sparse data more effectively, tailored specifically to the complexities of the problem domain.

## Software and Data

Complete project repository, including code used for generation of the simulated data, is to be made available upon

publication.

## Impact Statement

The PhysBR framework offers a data-efficient approach to reconstructing dense physical fields from sparse measurements by integrating machine learning with differentiable physics-based simulation, potentially benefiting domains such as environmental monitoring, fluid-dynamics-based engineering, and scientific experimentation where high-resolution data are costly or impractical to obtain. Its ability to enforce physical consistency may support more reliable scientific workflows and broaden access to advanced modeling in resource-limited settings, while also serving as an educational example of physics-guided machine learning.

At the same time, the method relies on the correctness of the assumed governing equations and simulation models, and incorrect or overly simplified physics may lead to plausible-looking but inaccurate reconstructions, particularly in high-stakes or out-of-distribution scenarios.

Although it raises no direct concerns regarding fairness or privacy, users should apply domain expertise and caution when interpreting outputs, recognizing that differentiable simulators introduce computational cost and that robustness under sparse sensing remains a key limitation. Overall, PhysBR contributes to the growing paradigm of combining analytical physical knowledge with modern ML, offering potential societal benefits while emphasizing the need for responsible and context-aware use.

## References

Akiba, T., Sano, S., Yanase, T., Ohta, T., and Koyama, M. Optuna: A next-generation hyperparameter optimization framework. In *Proceedings of the 25th ACM SIGKDD International Conference on Knowledge Discovery and Data Mining*, 2019.

Amorós-Trepot, M., Medrano-Navarro, L., Liu, Q., Guastoni, L., and Thuerey, N. Guiding diffusion models to reconstruct flow fields from sparse data, October 2025.

Ansel, J., Yang, E., He, H., Gimelshein, N., Jain, A., Voznesensky, M., Bao, B., Bell, P., Berard, D., Burovski, E., Chauhan, G., Chourdia, A., Constable, W., Desmaison, A., DeVito, Z., Ellison, E., Feng, W., Gong, J., Gschwind, M., Hirsh, B., Huang, S., Kalambarkar, K., Kirsch, L., Lazos, M., Lezcano, M., Liang, Y., Liang, J., Lu, Y., Luk, C., Maher, B., Pan, Y., Puhrsch, C., Reso, M., Saroufim, M., Siraichi, M. Y., Suk, H., Suo, M., Tillet, P., Wang, E., Wang, X., Wen, W., Zhang, S., Zhao, X., Zhou, K., Zou, R., Mathews, A., Chanan, G., Wu, P., and Chintala, S. PyTorch 2: Faster Machine Learning Through Dynamic Python Bytecode Transformation and Graph Compilation. In *29th ACM International Conference on Architectural Support for Programming Languages and Operating Systems, Volume 2 (ASPLOS '24)*. ACM, April 2024. doi: 10.1145/3620665.3640366. URL <https://docs.pytorch.org/assets/pytorch2-2.pdf>.

Baydin, A. G., Pearlmutter, B. A., Radul, A. A., and Siskind, J. M. Automatic differentiation in machine learning: A survey, February 2018.

Buhmann, M. D. *Radial Basis Functions: Theory and Implementations*. Cambridge Monographs on Applied and Computational Mathematics. Cambridge University Press, 2003.

Cressie, N. A. C. *Statistics for Spatial Data*. Wiley Series in Probability and Statistics. Wiley, 1 edition, September 1993. ISBN 978-0-471-00255-0 978-1-119-11515-1. doi: 10.1002/9781119115151.

Ehlers, S., Klein, M., Heinlein, A., Wedler, M., Desmars, N., Hoffmann, N., and Stender, M. Machine learning for phase-resolved reconstruction of nonlinear ocean wave surface elevations from sparse remote sensing data. *Ocean Engineering*, 288:116059, November 2023. ISSN 0029-8018. doi: 10.1016/j.oceaneng.2023.116059.

Ehlers, S., Stender, M., and Hoffmann, N. Bridging ocean wave physics and deep learning: Physics-informed neural operators for nonlinear wavefield reconstruction in real-time. *Physics of Fluids*, 37(10):107119, October 2025. ISSN 1070-6631, 1089-7666. doi: 10.1063/5.0294655.

Everson, R. and Sirovich, L. Karhunen–Loève procedure for gappy data. *JOSA A*, 12(8):1657–1664, August 1995. ISSN 1520-8532. doi: 10.1364/JOSAA.12.001657.

Fukami, K., Maulik, R., Ramachandra, N., Fukagata, K., and Taira, K. Global field reconstruction from sparse sensors with Voronoi tessellation-assisted deep learning. *Nature Machine Intelligence*, 3(11):945–951, November 2021. ISSN 2522-5839. doi: 10.1038/s42256-021-00402-2.

Glorot, X. and Bengio, Y. Understanding the difficulty of training deep feedforward neural networks. In Teh, Y. W. and Titterington, M. (eds.), *Proceedings of the Thirteenth International Conference on Artificial Intelligence and Statistics*, volume 9 of *Proceedings of Machine Learning Research*, pp. 249–256, Chia Laguna Resort, Sardinia, Italy, 13–15 May 2010. PMLR. URL <https://proceedings.mlr.press/v9/glorot10a.html>.

Holl, P. and Thuerey, N.  $\Phi_{\text{flow}}$  (PhiFlow): Differentiable simulations for pytorch, tensorflow and jax. In *International Conference on Machine Learning*. PMLR, 2024.

Huang, J., Yang, G., Wang, Z., and Park, J. J. Diffusion-pde: Generative pde-solving under partial observation. *Advances in Neural Information Processing Systems*, 37: 130291–130323, 2024.

Karniadakis, G. E., Kevrekidis, I. G., Lu, L., Perdikaris, P., Wang, S., and Yang, L. Physics-informed machine learning. *Nature Reviews Physics*, 3(6):422–440, May 2021. ISSN 2522-5820. doi: 10.1038/s42254-021-00314-5.

Koehler, F. Machine Learning and Simulation, 2024. URL <https://github.com/ceyron/machine-learning-and-simulation>.

Li, Z., Kovachki, N., Azizzadenesheli, K., Liu, B., Bhattacharya, K., Stuart, A., and Anandkumar, A. Fourier Neural Operator for Parametric Partial Differential Equations, May 2021.

Mano, Z., Kendler, S., and Fishbain, B. Information Theory Solution Approach to the Air Pollution Sensor Location–Allocation Problem. *Sensors*, 22(10):3808, May 2022. ISSN 1424-8220. doi: 10.3390/s22103808.

Mishra, K. V., Kruger, A., and Krajewski, W. F. Compressed Sensing Applied to Weather Radar, June 2014.

Murphy, B., Yurchak, R., and Müller, S. GeoStat-Framework/PyKrig: V1.7.3. Zenodo, October 2025.

Nebenzal, A., Fishbain, B., and Kendler, S. Model-based dense air pollution maps from sparse sensing in multi-source scenarios. *Environmental Modelling & Software*,

128:104701, June 2020. ISSN 13648152. doi: 10.1016/j.envsoft.2020.104701.

Oktay, O., Schlemper, J., Folgoc, L. L., Lee, M., Heinrich, M., Misawa, K., Mori, K., McDonagh, S., Hammerla, N. Y., Kainz, B., Glocker, B., and Rueckert, D. Attention U-Net: Learning Where to Look for the Pancreas, May 2018.

Raissi, M., Perdikaris, P., and Karniadakis, G. E. Physics informed deep learning (part i): Data-driven solutions of nonlinear partial differential equations. *arXiv preprint arXiv:1711.10561*, 2017.

Schmid, P. J. Dynamic mode decomposition of numerical and experimental data. *Journal of Fluid Mechanics*, 656: 5–28, August 2010. ISSN 0022-1120, 1469-7645. doi: 10.1017/S0022112010001217.

Strogatz, S. H. *Nonlinear Dynamics and Chaos: With Applications to Physics, Biology, Chemistry, and Engineering*. Chapman and Hall/CRC, New York, 3 edition, January 2024. ISBN 978-0-429-39849-0. doi: 10.1201/9780429398490.

Thess, A. Instabilities in two-dimensional spatially periodic flows. part i: Kolmogorov flow. *Physics of Fluids A: Fluid Dynamics*, 4(7):1385–1395, 1992.

Thuerey, N., Holzschuh, B., Holl, P., Kohl, G., Lino, M., Liu, Q., Schnell, P., and Trost, F. *Physics-based Deep Learning*. WWW, 2021. URL <https://physicsbaseddeeplearning.org>.

Virtanen, P., Gommers, R., Oliphant, T. E., Haberland, M., Reddy, T., Cournapeau, D., Burovski, E., Peterson, P., Weckesser, W., Bright, J., van der Walt, S. J., Brett, M., Wilson, J., Millman, K. J., Mayorov, N., Nelson, A. R. J., Jones, E., Kern, R., Larson, E., Carey, C. J., Polat, İ., Feng, Y., Moore, E. W., VanderPlas, J., Laxalde, D., Perktold, J., Cimrman, R., Henriksen, I., Quintero, E. A., Harris, C. R., Archibald, A. M., Ribeiro, A. H., Pedregosa, F., van Mulbregt, P., and SciPy 1.0 Contributors. SciPy 1.0: Fundamental Algorithms for Scientific Computing in Python. *Nature Methods*, 17:261–272, 2020. doi: 10.1038/s41592-019-0686-2.

Whitham, G. B. *Linear and Nonlinear Waves*. Pure and Applied Mathematics. Wiley-Interscience, New York, 1999. ISBN 978-0-471-35942-5 978-1-118-03120-9.

Wu, T. Y. T. Cavity and Wake Flows. *Annual Review of Fluid Mechanics*, 4(1):243–284, January 1972. ISSN 0066-4189, 1545-4479. doi: 10.1146/annurev.fl.04.010172.001331.

Zhang, Z. Improved adam optimizer for deep neural networks. In *2018 IEEE/ACM 26th international symposium on quality of service (IWQoS)*, pp. 1–2. Ieee, 2018.